

Dynamics of the Buckling Transition in Double-Stranded DNA and RNA

Katharina Ott,¹ Linda Martini,¹ Jan Lipfert,² and Ulrich Gerland^{1,*}

¹Physics of Complex Biosystems, Physics Department, Technical University of Munich, Garching, Germany and ²Department of Physics and Center for NanoScience, LMU Munich, Munich, Germany

ABSTRACT DNA under torsional strain undergoes a buckling transition that is the fundamental step in plectoneme nucleation and supercoil dynamics, which are critical for the processing of genomic information. Despite its importance, quantitative models of the buckling transition, in particular to also explain the surprising two-orders-of-magnitude difference between the buckling times for RNA and DNA revealed by single-molecule tweezers experiments, are currently lacking. Additionally, little is known about the configurations of the DNA during the buckling transition because they are not directly observable experimentally. Here, we use a discrete worm-like chain model and Brownian dynamics to simulate the DNA/RNA buckling transition. Our simulations are in good agreement with experimentally determined parameters of the buckling transition. The simulations show that the buckling time strongly and exponentially depends on the bending stiffness, which accounts for more than half the measured difference between DNA and RNA. Analyzing the microscopic conformations of the chain revealed by our simulations, we find clear evidence for a solenoid-shaped transition state and a curl intermediate. The curl intermediate features a single loop and becomes increasingly populated at low forces. Taken together, the simulations suggest that the worm-like chain model can account semiquantitatively for the buckling dynamics of both DNA and RNA.

SIGNIFICANCE Torsionally strained DNA, as is commonly found in the cell, can undergo a buckling transition to form plectonemic supercoils, which play critical roles in DNA processing. Single-molecule experiments have characterized the dynamics and stretching force dependence of the buckling transition for both double-stranded DNA and RNA and found a surprising two-orders-of-magnitude difference in the buckling timescales between the two molecules. We use Brownian dynamics simulations to predict the buckling dynamics and to understand the surprising difference between DNA and RNA. Our simulations also give access to the microscopic conformations of the chain that are inaccessible experimentally. Analysis of the simulations identified a curl intermediate that is increasingly populated at low stretching forces and might be observable experimentally.

INTRODUCTION

DNA stores the genetic information in all cellular life. The readout and maintenance of DNA generates torsional strains and DNA supercoiling (1–6). Conversely, twisting and bending strains of the DNA helix regulate many genomic processes (7,8). In the cell, DNA is organized in topological domains, operational units of the genome wherein DNA twisting and bending deformations cannot change independently (9,10). The interplay of bending and twisting fluctuations in \sim kb-length DNA and the associated dynamics are

thus fundamental for a biophysical understanding of genome readout and repair.

When torsionally strained, an initially linear stretch of DNA will eventually undergo a buckling transition, adopting bent and looped conformations, in which some of the torsional strain is released. The DNA buckling transition has been studied under precisely controlled conditions at the level of single molecules using magnetic and optical tweezers (11–13). These approaches control and monitor the configuration of single DNA molecules using the pairs of conjugate variables force-extension and torque-linking number. Single-molecule measurements have provided detailed information about many of the equilibrium properties of the buckling transition, such as the critical torque and linking number and the size of the initially formed loop, and about their dependencies on the applied stretching

Submitted August 21, 2019, and accepted for publication January 7, 2020.

*Correspondence: gerland@tum.de

Editor: Jason Kahn.

<https://doi.org/10.1016/j.bpj.2020.01.049>

© 2020 Biophysical Society.

force and solution conditions. In addition, recent measurements with magnetic and optical torque tweezers quantified the dynamics of the buckling transition. These experiments revealed that the characteristic timescale of DNA buckling depends on salt concentration, applied stretching force, and (weakly) on the DNA length and is in the range of 10–100 ms in tweezers experiments with micrometer-sized particles attached to the DNA (11–15). Experiments on double-stranded RNA found a similar buckling transition with equilibrium properties close to DNA but, surprisingly, an approximately two-orders-of-magnitude slower rate of buckling for RNA compared to DNA (14).

The timescale of buckling is believed to be rate limiting for the dynamics of DNA plectonemes, as a first direct measurement of plectoneme dynamics by fluorescent imaging (16) found that within the time resolution of the approach (20 ms), a plectoneme can disappear at one site and give rise to the formation of a new plectoneme several microns away along the chain. However, despite its biological relevance and increasingly detailed experimental characterization, the dynamics of DNA buckling are currently not understood on a quantitative level. The equilibrium properties of the buckling transition can be accounted for in the framework of a worm-like chain (WLC) model that describes double-stranded DNA or RNA as continuous, flexible rods with fixed bending and torsional stiffnesses (13,17,18). Daniels et al. extended the framework of the WLC model to the dynamics of the buckling transition by employing Kramer's theory to compute the buckling rate (19). For a WLC with homogeneous properties, this approach led to no energy barrier for buckling, in contrast to the experimental observations. After adding disorder due to intrinsic bending, an energy barrier was recovered, and buckling times in the range of 100 μ s were predicted, several orders of magnitude faster than the experimental observations. Although the discrepancy could be partially rationalized by the presence of micrometer-sized particles in the experimental setup, our current understanding of the dynamics of the nucleic acid buckling transition remains incomplete.

Here, we use Brownian dynamics simulations of a discretized WLC model to quantitatively analyze the buckling dynamics. Specifically, we ask whether a simple WLC description with the bending and torsional stiffnesses as the only mechanical parameters can account for the buckling dynamics of nucleic acids or whether anharmonic effects and/or structural transitions have to be taken into account. This question is also interesting in the light of several reports suggesting anomalous, “beyond WLC” flexibility of DNA on short length scales (20–24) that might facilitate buckling. A related salient question is how to explain the two-orders-of-magnitude difference in buckling rates between DNA and RNA, given that their bending and torsional rigidities differ by, at most, 20% (14). To address this question, we analyze the effect of these mechanical pa-

rameters on the buckling rate in our simulations. Finally, we focus on the conformations of the nucleic acid chain during the buckling transition. The literature suggests a “soliton” transition state (19,25) and a “curl” intermediate state (17,26). We inspect these states based on the joint distribution in the two-dimensional space of the writhe and extension observables, as well as on the corresponding conformations, as obtained from our simulations.

MATERIALS AND METHODS

We use a discretized WLC for the simulation of double-stranded DNA and RNA (27–31). The model corresponds to a bead-spring model consisting of $N + 1$ beads and N springs connecting the beads. The positions of the beads are denoted by \vec{r}_i , and the conformation of each spring is specified by its segment vector $\vec{s}_i = \vec{r}_{i+1} - \vec{r}_i$. To keep track of the twist in the conformation of the chain, we use an additional rotational orientation vector \vec{f}_i of unit length ($|\vec{f}_i| = 1$) for each segment, which is orthogonal to the segment direction $d\vec{e}_i = \vec{s}_i/|\vec{s}_i|$. By defining $\vec{g}_i = \vec{e}_i \times \vec{f}_i$ we obtain three orthonormal vectors spanning a local coordinate system for each segment (see Fig. 1 A). The following subsections introduce the energy functions, the boundary conditions, and the equations of motion that govern the dynamics of the discretized WLC model. Further subsections rationalize the parameter values used for our simulations (see also Table 1), define the observables calculated from the simulated trajectories, and discuss the rescaling procedure for comparison with experiments.

Energy functions of the model

The model describes all elastic properties of double-stranded DNA and RNA within the harmonic approximation. Each segment of the chain has an associated stretching energy

$$E_i^{(s)} = \frac{k_B T}{2(l_0 \delta)^2} (|\vec{s}_i| - l_0)^2, \quad (1)$$

where l_0 is the equilibrium spring length and δ is the stiffness parameter. The bending energy has a contribution from each consecutive pair of segments and depends on the bending angle β_i at bead i , defined via $\cos(\beta_i) = \vec{e}_i \cdot \vec{e}_{i-1}$ with $i = 1, \dots, N - 1$. The associated contribution to the total bending energy is

$$E_i^{(b)} = \frac{k_B T p_b}{2l_0} \beta_i^2, \quad (2)$$

where p_b is the bending persistence length. Similarly, the contribution to the torsional energy at bead i is given by

$$E_i^{(t)} = \frac{k_B T p_t}{2l_0} \theta_i^2, \quad (3)$$

where p_t is the torsional persistence length and the twist angle θ_i between the adjacent segments $i - 1$ and i can be calculated as (31)

$$\tan(\theta_i) = \frac{\vec{f}_i \cdot \vec{g}_{i-1} - \vec{g}_i \cdot \vec{f}_{i-1}}{f_i \cdot f_{i-1} + \vec{g}_i \cdot \vec{g}_{i-1}} \quad (4)$$

(see the Supporting Materials and Methods for a derivation). We describe electrostatic interactions between segments within the Debye-Hückel approximation (29) by placing λ point charges on each segment with even spacing. The charges are chosen so as to be consistent with the known effective charge density ν of DNA or RNA (see below). This leads to the electrostatic energy

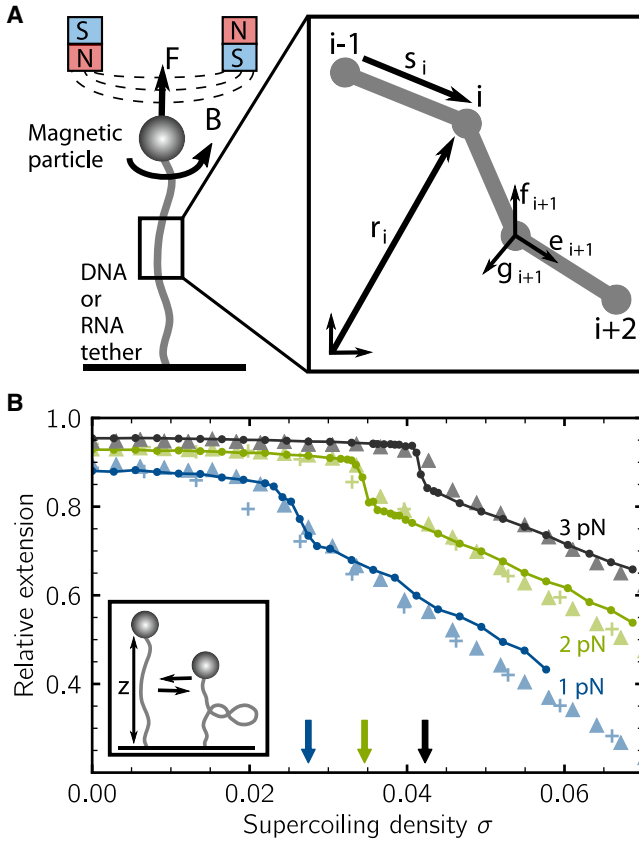


FIGURE 1 (A) Schematic representation of the basic experimental setup and the discretized WLC model. A magnetic particle is attached to a double-stranded DNA or RNA molecule. A stretching force is applied to the particle by magnetic tweezers, which are also used to rotate the particle, thus twisting the molecule. The magnification depicts the discretized polymer model together with the notation introduced in [Materials and Methods](#). (B) Quasiequilibrium response of DNA to supercoiling at different stretching forces is shown. The simulation data (*connected dots*) are obtained by averaging the DNA extension z over long simulation trajectories at fixed linking number and stretching force. The excess linking number Lk is rescaled to the supercoiling density σ (see [Materials and Methods](#)). Data for stretching forces of 1, 2, and 3 pN are shown as indicated. At a certain supercoiling density, the DNA buckles, abruptly forming a plectoneme, as illustrated in the inset. The buckling point is indicated by an arrow for each force. Crosses and triangles show experimental data from (14,33), obtained at the same forces, with 3.4 kb DNA at 100 mM NaCl (*triangles*) and 8 kb DNA with a phosphate-buffered saline buffer (*crosses*). To see this figure in color, go online.

$$E^{(el)} = \frac{\nu^2 l_0^2}{\epsilon \lambda^2} \sum_{m=1}^{\lambda N} \sum_{n=m+1+N_{es}}^{\lambda N} \frac{\exp(-\kappa r_{mn})}{r_{mn}} H(r_c - r_{mn}), \quad (5)$$

where E is the dielectric constant of the medium (water), r_{mn} is the distance between point charges m and n , and κ is the inverse Debye length. The sum excludes the interactions between the point charges on adjacent segments, as indicated by the offset N_{es} in the second summation range. The underlying rationale is that the effect of the interaction between adjacent segments is already included in the bending potential. To limit the computational cost incurred by the electrostatic energy, interactions with distant segments are neglected by introducing a cutoff at radius r_c via the Heaviside step function H . The cutoff radius is chosen such that the neglected forces are several or-

ders of magnitude smaller than the average value of any other force (31). Finally, we use the same method as (32) to avoid crossing of segments, i.e., we add an additional potential $E^{(rep)}$ that generates a strong repulsive force as soon as segments come closer than 2 nm, approximating the steric repulsion between double-stranded DNA or RNA segments.

Boundary and initial conditions

In the magnetic tweezer experiments, the DNA or RNA is attached with one end to a surface and with the other end to a micrometer-sized magnetic particle, which exerts a pulling force on the molecule. Because the particle is large on molecular scales, we can represent both of these boundaries as impenetrable flat surfaces in our model. We choose our coordinate system such that both of these surfaces are orthogonal to the z axis. The lower (fixed) surface is the x - y plane, and the position of the first bead is fixed to the origin. The upper surface moves with the z -coordinate of the last bead. In the experiments, the attachment of the molecule is such that no rotation is possible so that the torsional strain cannot relax at these points. Analogously, our model does not allow the first and last segment to rotate. This ensures that the linking number remains constant (see below), closely mimicking the situation in conventional magnetic tweezers with their high rotational trap stiffness (33). Explicitly accounting for the short-range repulsion of the impenetrable boundary surfaces on all inner beads of the chain ($i = 1, \dots, N - 1$) is also important for the conservation of the linking number because this prevents the chain from looping around one of its ends. We implement this with forces of the form

$$F_i^{(up)} = \begin{cases} 0, & (z_{N+1} - z_i) > 6L_b \\ -F_b \exp\left(-\frac{z_{N+1} - z_i}{L_b}\right), & 0 < (z_{N+1} - z_i) \leq 6L_b \\ -F_b, & (z_{N+1} - z_i) \leq 0 \end{cases} \quad (6)$$

for the upper surface and an analogous expression $F_i^{(low)}$ for the lower surface. Here, $L_b = 1$ nm is the characteristic length scale for the repulsion, and $F_b = 35$ pN is the repulsion force, chosen to be large enough that the chain cannot change its linking number. The stretching force exerted by the magnetic particle corresponds to an external force $F^{(ev)}$ in the positive z -direction, which we add to the total force acting on the last bead of the chain. Our model ignores the small lateral movement of the magnetic particle and allows the last segment to only move in the z -direction.

Our initial chain configuration is a straight line along the z axis. Because the vectors \vec{f}_i are used only to describe the relative twist of segments, the rotational angle of \vec{f}_0 for the first segment can be chosen arbitrarily. The remaining orientation vectors \vec{f}_i are then initialized relative to \vec{f}_0 ; e.g., for a chain that is initially untwisted, $\vec{f}_i = \vec{f}_0$. For a twisted initial configuration, with (excess) linking number Lk , we initialize the \vec{f}_i such that Lk turns are evenly distributed over all segments.

Brownian dynamics

The Brownian dynamics simulations of the discretized WLC model are based on the assumption of overdamped Langevin dynamics, in which each bead of the bead-spring model experiences a hydrodynamic drag that is calculated from Stokes law with a hydrodynamic radius a . Hydrodynamic interactions between the beads are neglected because they are computationally expensive and the effects of these interactions are typically small (30,31). These assumptions amount to an isotropic diffusion tensor,

$$D_{ij} = D_0 I \delta_{ij}, \quad (7)$$

TABLE 1 Parameters Used for the Simulation of Double-Stranded DNA and RNA Molecules

	Parameter	Symbol	Value DNA	Value RNA
Environment	Temperature	T	298 K	298 K
	Salt concentration	c_s	320 mM	320 mM
	Inverse Debye length	κ	1.261 nm^{-1}	1.261 nm^{-1}
	Viscosity	η	0.001 kg/s m	0.001 kg/s m
Chain	Dielectric constant water	ϵ	80	80
	Contour length	L	650 nm	650 nm
	Bending persistence length	p_b	45 nm	57 nm
	Torsional persistence length	p_t	90 nm	80 nm
Simulation	Segment equilibrium length	l_0	5 nm	5 nm
	Stretching stiffness parameter	δ	0.08	0.08
	Effective charge density	ν	$8.01e^-/\text{nm}$	$8.01e^-/\text{nm}$
	Point charges per segment	λ	3	3
	Excluded volume force	F_{rep}	35 pN	35 pN
	Bead hydrodynamic radius	a	1.6 nm	1.7 nm
	Rotational diffusion radius	r_{rot}	1.0 nm	1.2 nm
	Surface force length scale	l_b	1 nm	1 nm
	Surface force	F_b	35 pN	35 pN
	Time step	Δt	0.2 ns	0.2 ns

with $D_0 = k_B T / 6\pi\eta a$ the diffusion constant of a single bead and η the solvent viscosity. The hydrodynamic drag for the rotation of a segment about its longitudinal axis is estimated by assuming a cylinder with radius r_{rot} , which yields an approximate rotational diffusion coefficient of (30,34)

$$D_{rot} = \frac{k_B T}{4\pi\eta(r_{rot})^2 l_0}. \quad (8)$$

The simulations are based on a second-order Brownian dynamics algorithm (32,35,36). In this algorithm, the displacement after a time step Δt is calculated in two steps. In the first half step, the beads are displaced according to

$$\vec{r}'_i(t + \Delta t) = \vec{r}_i(t) + D_0 \frac{\vec{F}_i(t)}{k_B T} \Delta t + \vec{R}_i, \quad (9)$$

and the segments are rotated by the angles

$$\Delta\phi_i' = D_{rot} \frac{\Gamma_i(t)}{k_B T} \Delta t + \Phi_i. \quad (10)$$

Here, the total force \vec{F}_i on the i th bead is determined by analytically calculating the derivative of the potentials with respect to \vec{r}_i and adding the forces from the boundary conditions and the external stretching force,

$$\vec{F}_i = -\nabla_{\vec{r}_i} \left(\sum_j (E_j^{(s)} + E_j^{(b)} + E_j^{(t)}) + E^{(el)} + E^{(rep)} \right) \quad (11)$$

$$+ \left(F_i^{(up)} + F_i^{(low)} + F^{(ex)} \delta_{i,N+1} \right) \vec{e}_z, \quad (12)$$

where $\delta_{i,j}$ is the Kronecker delta symbol. Analogously, the total torque Γ_i is calculated by analytically differentiating the torsional energy with respect to ϕ_i ,

$$\Gamma_i = \partial_{\phi_i} \sum_j E_j^{(t)}. \quad (13)$$

The random displacements \vec{R}_i are drawn from a Gaussian distribution with the first and second moments

$$\langle \vec{R}_i \rangle = 0, \langle \vec{R}_i \otimes \vec{R}_j \rangle = 2D_0 \mathbf{I} \Delta t \delta_{ij}, \quad (14)$$

where \otimes denotes the outer product and \mathbf{I} the identity matrix. The random rotation angles Φ_i have a Gaussian distribution with

$$\langle \Phi_i \rangle = 0, \langle \Phi_i \Phi_j \rangle = 2D_{rot} \Delta t \delta_{ij}. \quad (15)$$

In the second half step, the bead positions are updated according to

$$\vec{r}_i(t + \Delta t) = \vec{r}'_i(t + \Delta t) + D_0 \frac{-\vec{F}_i(t) + \vec{F}'_i(t + \Delta t)}{2k_B T} \Delta t, \quad (16)$$

and the segments are rotated according to

$$\Delta\phi_i = D_{rot} \frac{-\Gamma_i(t) + \Gamma'_i(t + \Delta t)}{2k_B T} \Delta t. \quad (17)$$

Here, \vec{F}'_i and Γ'_i are the updated forces and torques calculated for the intermediate conformation specified by $\vec{r}'_i(t + \Delta t)$ and $\phi'_i(t + \Delta t)$. The orientation vectors \vec{f}_i and \vec{g}_i are updated at each half step by consecutively applying two rotation matrices. For instance, for the first half step, the first rotation matrix corresponds to a rotation about the axis $\vec{e}_i(t) \times \vec{e}'_i(t + \Delta t)$ by the angle between $\vec{e}_i(t)$ and $\vec{e}'_i(t + \Delta t)$, whereas the second corresponds to a rotation around $\vec{e}_i(t)$ by the angle $\Delta\phi_i'$.

We implemented the simulation algorithm in a custom C++ code and ran simulations in parallel on a standard CPU cluster (typically, a 3 s simulation trajectory required 3–4 weeks of CPU time). For Fig. 1, each data point is obtained from a simulation trajectory of at least 500 ms. We removed the initial transient period from each trajectory, during which the average extension (as obtained from a running average over 10^5 simulation steps) still changed. Once this running average remained within its standard deviation, we took the long time average over the remaining trajectory. At linking numbers close to the buckling transition, the molecule jumps forth and back between two relative extensions (on a timescale longer than 10^5 simulation steps). In these cases, we simulated until we observed at least three buckling transitions (in both directions) and averaged over the entire trajectory after the first buckling transition. For all remaining figures (which focus on the kinetics of the buckling transition), we simulated until we had at least three time traces with five full transitions (in both directions) each. For low forces, we simulated for 500 ms (resulting

in many transitions), whereas for high forces, we simulated for up to 3 s (just reaching our required five transitions).

Parameter choice

An overview of all parameters used in the simulations is given in Table 1 (for both double-stranded DNA and RNA). The contour length L of the molecules was chosen to match the minimal length of the molecules for which experimental data were available. Longer molecules would have been prohibitive in terms of computational cost, in particular with RNA parameters, for which the buckling transition is considerably slower than with DNA parameters. The stretching stiffness parameter δ was not set to match the experimentally measured stretching modulus but to a value that produced a stretching modulus 6–10 times softer than for real molecules (depending on the segment size used) to allow for larger simulation time steps. This choice was previously established as a good tradeoff between accuracy and computational cost for Brownian dynamics simulations of DNA within the force range that we consider here (30,31,37).

All parameters were chosen such that they describe experiments at room temperature and intermediate to high salt concentrations, with $[\text{Na}^+] = 320$ mM marking a typical experimental condition. For instance, the bending persistence length was set to the experimentally measured value at these conditions (14). The experimentally determined torsional persistence length depends on the applied stretching force (33,38). We chose the torsional persistence length to be consistent with the experiments of (33) and the simulation results of (18). The value for the effective charge density ν is taken from (29), and the number of point charges per segment, λ , was chosen such that the distance between charges is at most 2 nm. The radius used for the rotational diffusion coefficient r_{rot} is set to 1 nm, consistent with the radius of the DNA structure. The hydrodynamic radius a is calculated by demanding that in a straight configuration, the chain of beads has the same diffusion coefficient as a cylinder with the dimensions of DNA (30,31). Because the segment length l_0 strongly impacts the simulation time, its choice was a compromise between computational efficiency and accurate representation of the WLC model. By performing simulations with different segment lengths (Fig. S2), we identified a segment length of 5 nm as an acceptable compromise, which leads to buckling times that no longer show a significant dependence on segment length at modest stretching forces. For all simulations, we chose a time step Δt short enough to keep the typical increments in the positions of the beads and angles of the segments small. In particular, the probability for any rotation angle to change by more than π in an update is negligibly small.

In our model, the main differences between DNA and RNA are in the bending and torsional persistence lengths. For the effective charge density of RNA, we used the same value as for DNA. This may be an underestimate because RNA has a smaller distance between basepairs than DNA (0.28 nm vs. 0.34 nm). However, we expected the electrostatic interactions to play only a minor role at the given ionic conditions. To check this expectation, we ran two sets of test simulations for RNA at 2 pN stretching force with 1) an effective charge density that was a factor 0.34 nm or 0.28 nm \approx 1.2 higher than DNA and 2) the electrostatic interaction turned off entirely. Our simulations with the higher effective charge density resulted in a buckling time of 8.9 ± 1.7 ms, which agrees within the statistical error with the buckling time of 8.6 ± 2.5 ms obtained with the effective charge density of DNA. The result without electrostatic interactions, $\tau_{\text{buck}} = 9.8 \pm 1.9$ ms (using only hardcore repulsion), also agreed within the statistical error.

Observables

Our boundary conditions (see above) ensure that the ends of the WLC cannot rotate and also that the chain cannot move around its end points. Therefore, the excess linking number Lk , defined as the number of turns between the upper and lower ends of the chain, is an invariant of the dynamics. At each point in time, the extension z of the WLC is defined by its $z_N + 1$

coordinate. In the simulation, we track both the extension and the writhe Wr . We compute the writhe in two independent ways (39): first, by employing the relation

$$Wr = Lk - Tw \quad (18)$$

between writhe, excess linking number, and twist, Tw . The calculation of twist for helical nucleic acids can be complicated by the fact that one needs to distinguish between the local basepair property twist and the global twist of the helix (40). The popular tools for the analysis of all-atom molecular dynamics simulations (41,42) are not applicable here because our model has no explicit representation of the bases. Instead, we compute the total twist as a sum over all twist angles of the discretized WLC (30),

$$Tw = \frac{1}{2\pi} \sum_{i=2}^N \theta_i. \quad (19)$$

To ensure that no segments have overlapped, we also calculate the writhe explicitly every thousandth time step of the simulation, using the method referred to as “Method 1a” in (39). In the rare cases in which the two calculated values of the writhe did not agree (typically once in 10^7 time steps, depending on Lk and the external force), we restarted the simulation from the saved configuration at the last successful check. The independent calculation of the writhe is also a validation of our calculation of the twist.

The equilibrium response is obtained from simulations started at a given Lk and stretching force $F^{(ex)}$ and run until they have equilibrated, as judged by the convergence of the mean extension. To compare the simulation data to a wide range of experiments with molecules of different contour lengths, length-independent quantities were introduced. The relative extension is defined as the extension z divided by the contour length L of the molecule. The supercoiling density σ is defined as the excess linking number Lk divided by the number of intrinsic turns of the double helix (one turn for 10.5 bp for DNA). The distribution histogram of the extension can be fitted with a double Gaussian. The weight of the Gaussian describing the postbuckling state is the probability to be in the postbuckling state p_{post} (Fig. 2 A). The dependence of p_{post} on Lk is fitted to the expression (13)

$$p_{\text{post}} = \frac{1}{1 + \exp\left(\frac{(Lk_{\text{buck}} - Lk)(2\pi)^2 \Delta Wr_{\text{buck}}}{k_B T}\right)}, \quad (20)$$

where Lk_{buck} and ΔWr_{buck} are used as fit parameters. Equation 20 is obtained by expressing the energy of the prebuckling state by the energy stored in twist and the energy of the postbuckling state by the energy stored in twist plus the energy stored in the plectoneme. The probability to be in the postbuckling state then follows from Boltzmann statistics, with Lk_{buck} defined as the point at which the pre- and postbuckling states are equally populated (this definition of Lk_{buck} eliminates the term for the energy stored in the plectoneme). The parameter Lk_{buck} is referred to as the buckling point, and it corresponds to the linking number at which the probabilities for the WLC to be in the prebuckling or the postbuckling state are equal (Fig. 2 B). The parameter ΔWr_{buck} corresponds to the change in writhe at the buckling point. The mean of each Gaussian in the extension distribution describes the mean extension of the DNA strand in the respective state. The dependence of the mean extensions of the pre- and postbuckling states on the linking number are fitted with a linear function (shown in Fig. 2 C). The difference between these extensions evaluated at the buckling point $Lk = Lk_{\text{buck}}$ is referred to as the jump size Δz_{buck} (Fig. 2 C).

For the analysis of the dynamics of the buckling transition, we obtain the dwell times in the pre- and postbuckling states from simulation trajectories in the writhe coordinate. The writhe coordinate is particularly well suited to separate between the pre- and postbuckling states, as seen from the writhe histogram (Fig. 2 A). The writhe trajectories are smoothed using a running average of 10^4 simulation steps, corresponding to 2 μ s in real time. The

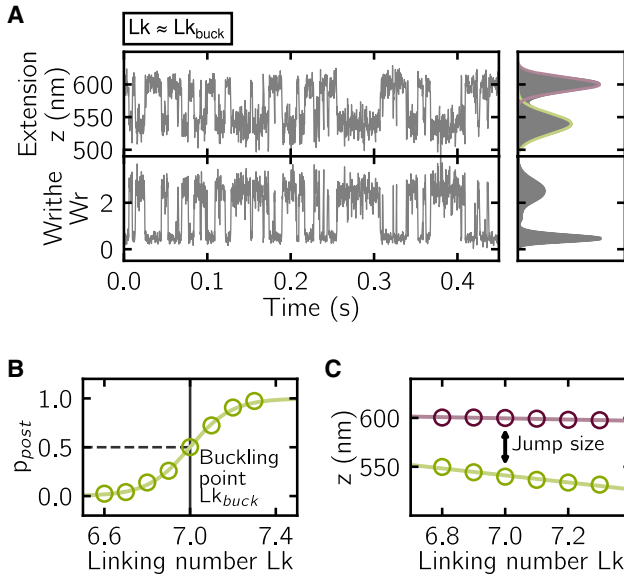


FIGURE 2 Simulation of a 650 nm DNA at 2.5 pN stretching force. (A) Time traces of the extension and writhe at an excess linking number of $Lk = 7.0$ close to the buckling point are shown. The corresponding extension and writhe histograms are shown on the right. (B) The probability of DNA to be in the postbuckling state (green circles) is shown. The light green line shows a fit with Eq. 20. (C) Mean extensions of DNA in the pre- and postbuckling states as a function of the excess linking number are shown. The lines indicate linear fits. The jump size is defined as the difference between the fit functions evaluated at the buckling point. To see this figure in color, go online.

minimum between the peaks in the writhe histogram is used as a threshold to calculate the dwell times, which are distributed exponentially (Fig. 3 A). Averaging these dwell times gives the average dwell time (Fig. 3 B). The average dwell times are expected to depend exponentially on Lk according to (13)

$$\tau_{\text{pre}} = \tau_{\text{buck}} \exp\left(-\frac{(2\pi)^2 p_l}{L} (Lk_{\text{buck}} - Lk) \Delta W r_{\text{buck}} / k_B T\right) \quad (21)$$

and an analogous expression for the postbuckling state. The intersection of the two exponential functions describing the pre- and postbuckling state then defines the buckling time τ_{buck} (Fig. 3 B).

Rescaling of the buckling time

To compare the timescale of the simulated buckling events to the absolute timescale of the experimental data, we have to account for the presence of the magnetic particle in the experiment, which is not explicitly included in the model. Furthermore, we also have to take into account that the contour length L of the DNA or RNA in the simulation is often shorter (for computational efficiency) than the molecules used in experiments. Therefore, we rescaled the simulated buckling times τ_{sim} proportionally, by the ratio of the estimated total hydrodynamic drag coefficient of the experimental system (DNA and magnetic particle) to that of the model system, to obtain the rescaled buckling time

$$\tau_{\text{rescaled}} = \tau_{\text{sim}} \frac{\gamma_{\text{DNA,exp}} + \gamma_{\text{MP}}}{\gamma_{\text{DNA,sim}}} \quad (22)$$

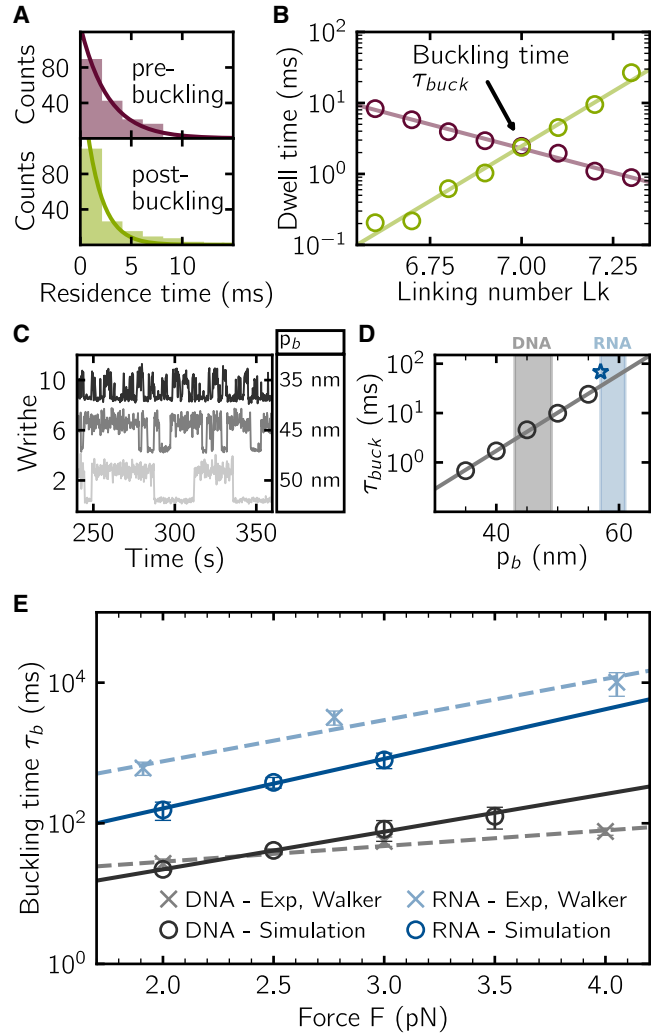


FIGURE 3 Dynamics of the buckling transition. (A) Histograms of dwell times in the pre- and postbuckling states (DNA parameters, linking number 7.0) with superimposed exponential fits (solid lines) are shown. (B) Definition of the buckling time is shown. Mean dwell times in the prebuckling (purple circles) and postbuckling (green circles) states are plotted as a function of the linking number, with the solid lines indicating exponential fits. The intersection of the lines defines the buckling time τ_{buck} . (C) Time traces of the writhe dynamics at different bending persistence lengths p_b are shown. (D) Buckling time as a function of the bending persistence length at a fixed stretching force of 3 pN is shown. The data points from simulations (circles) are well described by an exponential fit (solid line). The shaded gray area marks the range of experimentally measured values for the bending persistence length of DNA (11,14,33,50,51), and the blue area marks the corresponding range for RNA (14,51). The simulated buckling time obtained with our RNA parameters is indicated by the blue star. (E) Buckling time of DNA and RNA for different external forces are shown. Simulation data (circles) were rescaled for better comparison to experimental data (crosses). The experimental data are taken from (15). The lines show exponential fits to the experimental (dashed lines) and simulation (solid lines) data. To see this figure in color, go online.

Here, $\gamma_{\text{DNA,exp}}$ is the (Stokes) drag coefficient of the molecule used in the experiment, γ_{MP} is the drag coefficient of the magnetic particle, and $\gamma_{\text{DNA,sim}}$ is the drag coefficient of the simulated WLC. The rescaled buckling times (Eq. 22) are then directly comparable to the experimentally determined buckling time values. The physical assumption underlying Eq. 22 is

that of an effective one-dimensional reaction coordinate for the buckling transition. Given that the z -extension changes during the transition, we assume that essentially the entire system (DNA and magnetic particle) moves during the transition and thus use the total drag coefficient in Eq. 22.

The drag coefficient for the molecule in the experiment is estimated as $\gamma_{\text{DNA,exp}} = 2\pi\eta z/\ln(z/b)$, where z is the extension of the molecule and $b = 2$ nm its diameter (43). For the estimation of the drag of the magnetic particle γ_{MP} , we take into account that the particle is close to the flow cell surface, which influences its hydrodynamic drag. We include this effect within the Faxén approximation (44). Because we neglected hydrodynamic interactions, we expected that our simulations would display a linear scaling of the buckling time with the contour length L of the simulated molecule. To test this expectation, we simulated chains with different contour lengths. For DNA parameters, the simulations show a clear linear dependence of the buckling time on L (see Fig. S3). For RNA parameters, the buckling time is much longer, requiring simulations at high computational cost. We therefore obtained fewer buckling events, resulting in larger statistical errors in the average buckling time. The associated scaling behavior in Fig. S3 is not as clear-cut as in the case of DNA parameters but nevertheless consistent with linear scaling. Hence, we assumed a linear dependence of the simulated buckling time on the contour length for both DNA and RNA, which is taken into account in the drag coefficient $\gamma_{\text{DNA,sim}}$. For more details and a comparison to experimental results, see the caption of Fig. S3.

RESULTS AND DISCUSSION

Our central aim is to study the dynamics of the buckling transition in double-stranded DNA and RNA within the WLC model. We also want to clarify whether the surprisingly large difference in the experimentally observed buckling dynamics of DNA and RNA can be rationalized just from the difference in their physical polymer properties, in particular their torsional and bending rigidities. Toward this end, we describe both DNA and RNA by a bead-spring model with harmonic potentials for stretching, bending, and twisting, i.e., a discretized WLC model; see Fig. 1 A for illustration and Materials and Methods for details. To monitor the buckling dynamics, we performed Brownian dynamics simulations and recorded time traces of the chain extension and the writhe. In the experiment, as well as in the simulations, the control parameters are the applied force (experimentally controlled by the gradient of the magnetic field) and the linking number (experimentally controlled by the number of turns of the magnetic particle). The magnetic particle in the experiment has two essential effects on the dynamics of the chain: 1) because of its hydrodynamic drag, it considerably slows all motion that changes the total extension of the chain; and 2) because of its size, it confines the motion of the chain. For computational efficiency, we do not explicitly simulate the magnetic particle but instead account for these two effects indirectly via 1) a rescaling of the simulated buckling time according to Eqs. 22 and 2) an (upper) boundary condition that confines the motion of the chain. Both boundaries, i.e., the magnetic particle and the (lower) surface to which the chain is attached, are modeled as horizontal surfaces with fixed repulsion forces. Importantly, these repulsion forces prevent release of torsional strain by loop passage around the endpoints of the chain.

We also incorporate a sufficiently strong self-repulsion of the chain, which prevents crossing of chain segments. Together, the boundary condition and self-repulsion ensure that the externally controlled linking number remains conserved.

The ionic conditions of the surrounding solvent enter the model via the effective charge density of the chain and the Debye screening length for electrostatic interactions, whereas the solvent temperature primarily affects the strength of the stochastic forces (see Materials and Methods). Given that the system is in the regime of very low Reynolds numbers, the motion of the chain is overdamped, and the primary effect of the solvent on the chain is the hydrodynamic drag. We neglect solvent-mediated long-range hydrodynamic interactions between the beads, which typically have only a minor effect on the dynamics (30,31). All parameters that enter the simulations for DNA and RNA are summarized in Table 1.

Coarse-grained Brownian dynamics simulations reproduce equilibrium parameters of the buckling transition

To validate our model, we first characterized the equilibrium properties of its buckling transition. We used the parameters for double-stranded DNA and performed simulations with different fixed linking numbers, at different constant stretching forces. At each linking number Lk , we recorded a long time trace of the extension to obtain the average extension $\langle z \rangle$; see Materials and Methods for the simulation procedure. Fig. 1 B shows the resulting average extension as a function of the linking number (*connected dots*) for three different stretching forces (1, 2, and 3 pN). Note that in this graph, both the extension and the linking number are rescaled to length-independent quantities (see below). The extension initially stays approximately constant with increasing linking number. However, at a critical linking number, the curves display a distinct and rapid decrease in the average extension. At this point, the simulated DNA undergoes a buckling transition from a linear conformation to a plectonemic conformation (*inset* of Fig. 1 B). When the stretching force is increased, the buckling transition becomes sharper. Concomitantly, the associated critical linking number Lk_{buck} becomes larger; see the arrows in Fig. 1 B, which mark the buckling transition for each stretching force (see below for the precise definition of the critical linking number). In the postbuckling regime, further increase of the linking number causes a linear decrease in extension as the remaining stretched DNA is gradually converted into plectonemic DNA.

Fig. 1 B also shows several experimental data sets (14,33) for stretching forces of 1, 2, and 3 pN (*triangles* and *crosses*; see caption for the experimental conditions). In these experiments, the linking number is slowly increased by rotating the magnetic field. The measured extension, recorded by

optical tracking of the magnetic particle, then corresponds to a quasiequilibrium value. Because the experiments were run with DNA molecules of different contour lengths, we rescaled the excess linking number Lk to the supercoiling density σ , an intensive variable (see [Materials and Methods](#)). Likewise, we rescaled the extension to relative extension. Furthermore, to take into account the experimental uncertainty in the absolute z -position, we allowed the extension axis of the experimental data to be shifted by up to 150 nm for each data set. The simulated data are in good agreement with the experimental data ([Fig. 1 B](#)), suggesting that the WLC model can quantitatively account for the (quasi)equilibrium response of DNA under torsional strain, including the buckling transition, consistent with previous theoretical studies ([18,45](#)).

To study the buckling transition displayed by our simulated DNA in more detail, we focused on the linking number regime in which the transition occurs. We analyzed long time traces of the extension as well as the writhe Wr defined in [Eq. 18](#). In the transition regime, the DNA hops back and forth between the prebuckling state (linear conformation) and the postbuckling state (plectonemic conformation), as seen in the time traces of [Fig. 2 A \(left\)](#). From these time traces, we obtain the associated histograms of the extension z and the writhe Wr (see [Fig. 2 A, right](#)). The extension histogram displays a distinct two-state behavior, with two peaks corresponding to the pre- and postbuckling states. This distribution is well described by a double-Gaussian fit (*colored lines* in [Fig. 2 A, right](#)). The double-Gaussian fit to the extension distribution can be used to define Lk_{buck} , the critical linking number that marks the buckling point, in the same way as for experimental data ([13,15](#)): for each linking number Lk , the weights of the Gaussian peaks yield the probabilities to be in the pre- and postbuckling states, and the buckling point is reached when these probabilities are equal. [Fig. 2 B](#) shows the probability p_{post} to be in the postbuckling state as a function of the excess linking number Lk over the range of the transition. In this figure, the buckling point Lk_{buck} corresponds to the excess linking number at which $p_{\text{post}} = 0.5$, as indicated by the lines.

The double-Gaussian fit also yields the mean extensions associated with the pre- and postbuckling states (see [Fig. 2 C](#)). The “jump size” Δz of the buckling transition is then defined as the difference between the mean extension of the prebuckling state and the mean extension of the postbuckling state, evaluated at the buckling point, as indicated in [Fig. 2 C](#). All of these observables constitute equilibrium properties of the buckling transition and can be measured experimentally. [Fig. S1](#) shows a direct comparison of the simulation results to the corresponding experimental values for a number of different equilibrium properties as a function of the stretching force: the buckling point Lk_{buck} , the widths of the two peaks in the extension distribution, the jump size Δz , and also an estimate of the change in writhe ΔWr_{buck} at the buckling transition. Because writhe cannot

be measured directly in the experiment, the latter is based on an energetic model of the buckling transition ([13](#)) that predicts the functional dependence of p_{post} on the linking number, with a parametric dependence on ΔWr_{buck} , Lk_{buck} , the torsional persistence length p_t , the contour length L , and the temperature T ; see [Eq. 20](#) in [Materials and Methods](#) and ([13](#)) for details. The model captures the experimentally observed equilibrium behavior quantitatively ([Fig. S1](#)). Taken together with the agreement observed above in [Fig. 1 B](#), this strongly suggests that our Brownian dynamics simulations of the discretized WLC model yield a valid description of the static properties of the buckling transition.

Buckling dynamics is highly sensitive to bending rigidity but not to torsional rigidity

Next, we used the Brownian dynamics approach to analyze the dynamics of the buckling transition in the discretized WLC model. Given that within our model, the only essential differences between double-stranded RNA and DNA are in the magnitudes of the bending persistence length p_b and the torsional persistence length p_t , we were especially interested in the dependence on these parameters. To obtain the kinetic rate constants associated with the buckling transition, we analyzed long simulation trajectories with a two-state model, assigning each point on a trajectory to be in either the prebuckling state or the postbuckling state. Because the writhe histogram displays a very pronounced minimum, we performed the state assignment by setting a threshold for the value of the writhe coordinate at this minimum. From these data, we constructed histograms of dwell times in the pre- and postbuckling states (see [Fig. 3 A](#)). These histograms take on a simple exponential form, consistent with experiments ([13,15](#)). We therefore used a single-exponential fit to these histograms to extract the decay rates k and the associated average dwell times $\tau = 1/k$.

The dwell time in the prebuckling state decreases exponentially with the linking number, whereas the dwell time in the postbuckling state increases exponentially with the linking number ([Fig. 3 B](#)). This is in agreement with experimental observations ([13,15](#)) and with [Eq. 21](#). At a certain critical linking number, the dwell times of the pre- and postbuckling states are equal. This occurs precisely at the linking number Lk_{buck} that corresponds to the buckling point ([Figs. 2 B](#) and [3 B](#)), confirming that the static and dynamic definitions of the transition point are consistent. The buckling time, τ_{buck} , is then defined as the single dwell time at this unique point ([Fig. 3 B](#)).

For a given set of parameters, the buckling time τ_{buck} is the characteristic timescale associated with the buckling dynamics. To characterize the parameter dependence of the buckling dynamics, we varied the bending persistence length p_b and the torsional persistence length p_t . We found

a strong dependence of τ_{buck} on the bending persistence length p_b , which is well described by an exponential fit (Fig. 3, C and D). In contrast, we found only a weak dependence of τ_{buck} on p_t , with the buckling time decreasing slightly as the torsional persistence length is increased (Fig. S5).

To rationalize the observed sensitivity of the buckling dynamics on the bending persistence, we considered a kinetic model based on a soliton-like transition state (19) (see Supporting Materials and Methods for details). This model predicts that the energy barrier for buckling increases with the bending persistence length, consistent with the intuitive expectation that the higher the bending stiffness, the more energy is needed to form loops or solitons. On a quantitative level, the kinetic model captures the observed dependences of the buckling time on all parameters relatively well, although it overestimates the effect of all polymer properties on the buckling time (Fig. S4).

Polymer properties account for a large fraction of the experimentally observed difference between DNA and RNA buckling dynamics

Because the polymer properties have a significant effect on the buckling dynamics, we asked whether this dependence alone might be able to account for the different buckling times observed experimentally for DNA and RNA (15). To quantitatively compare simulations with experimentally determined buckling times, simulations were run with DNA and RNA parameters (Table 1) at different external forces. To be able to compare the simulated buckling times to the experimental data, the simulation data were rescaled according to Eq. 22 to account for the hydrodynamic drag of the magnetic particle and the difference in contour lengths between simulation and experiment. Fig. 3 E shows the resulting comparison, with the experimental and simulated buckling times τ_{buck} plotted as a function of the stretching force F for both DNA and RNA. The qualitative trend that the buckling dynamics of RNA is much slower than for DNA is displayed by both the experimental and the simulation data.

For a more quantitative comparison, we focused on features that do not depend on our rescaling procedure, which necessarily produces some level of uncertainty in the absolute timescale of the buckling times (see Materials and Methods). Because the buckling times increase roughly exponentially with the stretching force, we fitted exponential functions of the form

$$\tau_{\text{buck}} = \tau_0 \exp\left(\frac{F \Delta x}{k_B T}\right) \quad (23)$$

to both the experimental and the simulated data, with τ_0 and Δx as fit parameters (Fig. 3 E). For the case of DNA, the parameter Δx , which characterizes the force dependence

of the buckling times, is higher for the simulated data ($\Delta x = 5.0 \pm 0.5$ nm) than for the experimental data ($\Delta x = 2.1 \pm 0.4$ nm). In contrast, for the case of RNA, the simulations lead to a value of $\Delta x = 6.6 \pm 1.5$ nm, which is consistent with the experimental value of $\Delta x = 5.5 \pm 1.1$ nm. Here, to estimate the error of Δx , we split the time traces into five (DNA at 2, 2.5, and 3 pN, RNA at 2 pN) or three (remaining cases) sections and calculated the standard deviation of the buckling times obtained from these sections. The discrepancy between the Δx -values for DNA between experiment and model is in part due to the discretization of the WLC model: at higher stretching forces, the more bendable DNA structures yield plectonemes with very small end loops, which are not well resolved when the segment length is not much smaller than the end-loop size. We tested this effect by calculating Δx for different segment lengths and found that Δx indeed increases with increasing segment size (Fig. S2). However, our discretization is sufficient to make discretization effects negligible for DNA at forces of 2.5 pN or smaller (Fig. S2). For RNA discretization, the effects are smaller because of the larger bending persistence length.

Another scaling-independent quantity is the ratio of the buckling times for RNA and DNA, which we denote by $r = \tau_{\text{RNA}}/\tau_{\text{DNA}}$. At 2 pN stretching force, the experimental value is $r = 40$, whereas the value obtained from our simulations is $r = 7$. On the logarithmic scale, the discretized WLC model thus accounts for more than half of the experimental effect (Fig. 3 E). Because the buckling time is strongly affected by small changes in the bending persistence lengths, the precise values used for DNA and RNA matter for the model prediction of the r -value. A better agreement with the experimental value of $r = 40$ could be reached if the bending persistence lengths for RNA and DNA are allowed to be varied within the range of experimentally measured values (Fig. 3 D). Nevertheless, the WLC cannot fully rationalize the observed difference between DNA and RNA, suggesting a possible role for other effects (see Conclusions).

Conformations along the buckling transition

Our simulations enable us to probe the detailed conformations of the chain that are associated with the buckling transition and that are not directly observable experimentally. Toward this end, we ran simulations with DNA parameters at stretching forces of 1–3 pN (with the linking number adjusted to the buckling point), again tracking writhe and extension but also saving the entire conformation of the chain every 1000 time steps. For all forces, the writhe coordinate separates the states more clearly than the extension, as seen from the writhe and extension histograms in Fig. 4 (for $F = 1$ pN and $F = 3$ pN) and Fig. S7 (for $F = 2$ pN). To leverage the full information contained in the writhe and extension data, we determined the joint distribution in

the two-dimensional space of writhe and extension (Figs. 4, C and G and S7).

At the highest stretching force (3 pN), the system displays two clear and well-separated peaks in the writhe-extension distribution (Fig. 4 C), consistent with the effective two-state behavior observed in previous studies, e.g., in (13–15). The peak associated with the postbuckling state is considerably broader than the peak associated with the prebuckling state, in line with experimental observations (15). Fig. 4 D displays three representative conformations of the WLC at the marked points in the writhe-extension histogram. The conformation associated with the prebuckling state is identified as essentially straight, whereas the conformation from the postbuckling state has a clear plectonemic form (13,26). The conformation from the transition state has a solenoidal shape resembling the previously described form referred to as “soliton” (19,25,26). Fig. S6 shows three different conformations of the transition state, which all take on a similar shape.

At the lowest force (1 pN), the peaks in the writhe-extension distribution are significantly broader (Fig. 4 G), consistent with the broadening at low forces observed experimentally (15). Closer inspection suggests that an additional intermediate state exists in this force regime,

which is also faintly discernible already at 2 pN stretching force (Fig. S7). Fig. 4 H shows four representative conformations of the WLC at the marked points in the writhe-extension histogram. In between the soliton transition state and the plectoneme state, there is now an intermediate state with a conformation that features only one loop and resembles the “curl” state that was previously described; see (17,26) and references therein. This intermediate state can also be observed in the writhe histogram (Fig. 4 E), but not in the extension histogram (Fig. 4 F). We used a Gaussian mixture model to extract estimates for the population of the curl and plectoneme states from the writhe histograms for different linking numbers and stretching forces. This analysis shows that for the simulation with 1 pN stretching force (at the corresponding buckling point of $Lk = 4.7$), the curl state is more populated (at 38.6%) than the plectonemic state (at 29.2%). Fig. S8 plots the fractional populations of the curl and plectoneme states as a function of linking number for different stretching forces. For the higher forces, the curl state is barely populated, and the WLC only passes through the curl state to form a plectoneme. Overall, the Gaussian mixture model indicates that the curl state becomes more populated relative to the plectonemic state at low forces and linking

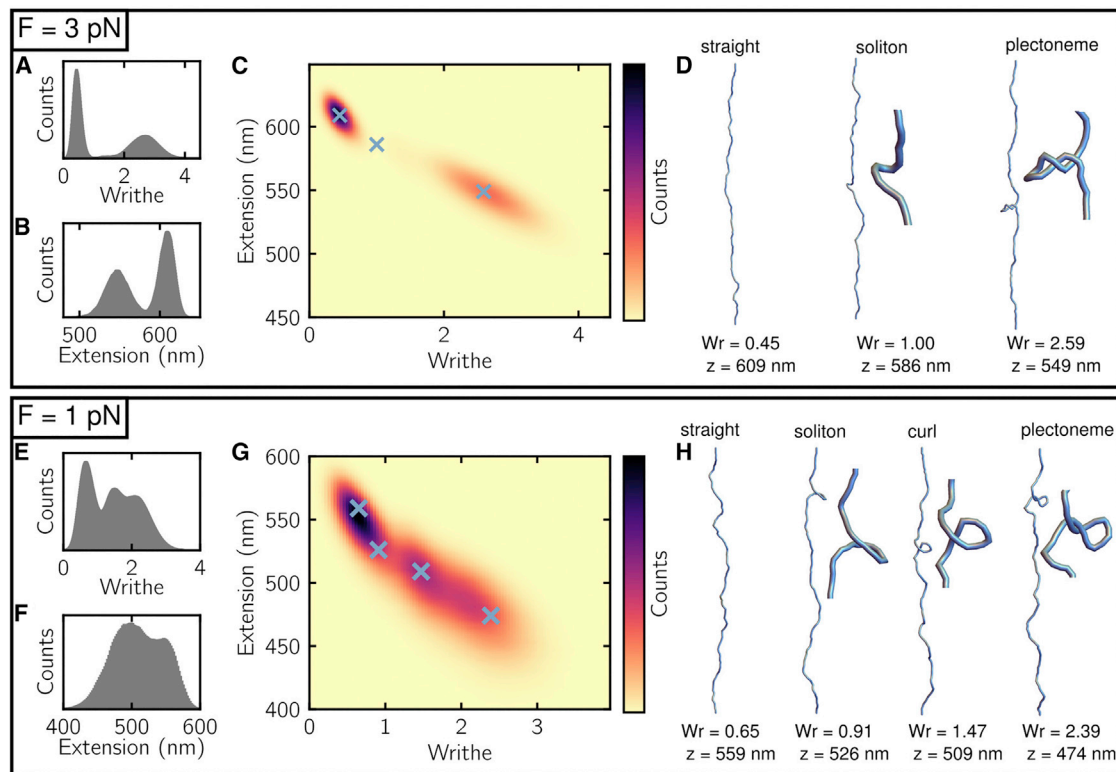


FIGURE 4 Configurations adopted during the buckling transition. (A–D) Simulations at the buckling point with a stretching force of $F = 3$ pN and DNA parameters are shown. The writhe distribution (A) and the extension distribution (B) are projections of the joint distribution (C) in the two-dimensional writhe-extension space. (D) Snapshots of representative configurations in the pre- and postbuckling states and the transition state, with the associated writhe and extension coordinates marked by crosses in (C), are given. (E–H) The same is given for a stretching force of $F = 1$ pN. At this lower force, an additional intermediate state appears that displays a “curl” conformation. To see this figure in color, go online.

numbers below the buckling point. This is in agreement with theoretical predictions, according to which the increase in the population of the curl state at lower forces is due to a reduced energy cost for loop formation (13,17). By introducing mismatches in the DNA, which reduces the looping energy, signatures of such a curl state have even been observed experimentally (26).

CONCLUSIONS

We took a Brownian dynamics approach based on a discretized WLC chain model to study the dynamics of the buckling transition in double-stranded RNA and DNA. We first established that known equilibrium properties of the buckling transition are quantitatively reproduced from long simulation trajectories. We then analyzed the kinetics of the transition between the straight and the plectonemic conformation, finding semiquantitative agreement with experimental data. In particular, our simulations have shown that the WLC model can partially account for the large difference in the experimentally observed buckling times for DNA and RNA. The difference in the simulated buckling times can mainly be attributed to the difference in bending persistence length between DNA and RNA, as our simulations show a strong dependence of the buckling time on the bending persistence length.

In total, the WLC model can account for roughly a sevenfold difference between the buckling times of DNA and RNA using the parameters listed in Table 1. This leaves a factor of about six in the fold change between DNA and RNA buckling times unexplained. Because there is some uncertainty in the experimentally determined persistence lengths of DNA and RNA, this remaining factor could be partially explained by the WLC model, if our parameter sets underestimate the difference in the bending persistence lengths of DNA and RNA. However, even if this is the case, a discrepancy of at least two- to threefold likely remains. This discrepancy could be due to a number of factors not included in the discretized WLC model, such as anisotropic bending and twist-bend coupling (46,47), anharmonic and nonuniform (sequence-dependent) elastic properties (21), and local melting of the double-helical structure (48,49). Additionally, our simplified treatment of the electrostatic interactions and our neglect of hydrodynamic interactions may contribute to this discrepancy. A detailed investigation of these factors will require a precise determination of the parameters involved and is beyond the scope of this work.

A benefit of the simulation approach is that it permits monitoring the full conformational dynamics of the molecules during the buckling transition, in contrast to experiments, in which typically only the extension is monitored directly. (Although recent approaches for direct torque and twist measurements are available (11,38), their temporal resolution in the torque or twist coordinate is typically much lower than in the extension degree of freedom.) We

kept track of the writhe observable in all simulations and found that this observable separates well between the conformational states of the WLC. This became apparent in particular when we sampled conformations of the WLC during the buckling transition at different points in the two-dimensional writhe-extension space (Fig. 4). This analysis showed that at forces higher than ~ 2 pN, the coarse-grained dynamics of the buckling transition can be represented as a transition from the straight conformation in the prebuckling state via a “soliton” transition state to the plectonemic conformation of the postbuckling state. At lower forces (~ 1 pN), an intermediate “curl” state appears, consistent with prior theoretical predictions and experimental indications (see (17,26) and references therein). Taken together, our study consolidates the WLC model as a model that describes not only the static properties but also the dynamics of the torsionally induced buckling of both double-stranded DNA and RNA on a semiquantitative level.

SUPPORTING MATERIAL

Supporting Material can be found online at <https://doi.org/10.1016/j.bpj.2020.01.049>.

AUTHOR CONTRIBUTIONS

All authors designed research. K.O. performed research. All authors analyzed data. K.O., J.L., and U.G. wrote the manuscript.

ACKNOWLEDGMENTS

We thank Willem Vanderlinden and Philipp Walker for useful discussions.

This work was funded by the Deutsche Forschungsgemeinschaft (DFG, German Research Foundation)-SFB863-111166240.

REFERENCES

1. Liu, L. F., and J. C. Wang. 1987. Supercoiling of the DNA template during transcription. *Proc. Natl. Acad. Sci. USA.* 84:7024–7027.
2. Borukhov, S., and E. Nudler. 2003. RNA polymerase holoenzyme: structure, function and biological implications. *Curr. Opin. Microbiol.* 6:93–100.
3. Cozzarelli, N. R., G. J. Cost, ..., J. E. Stray. 2006. Giant proteins that move DNA: bullies of the genomic playground. *Nat. Rev. Mol. Cell Biol.* 7:580–588.
4. Koster, D. A., A. Crut, ..., N. H. Dekker. 2010. Cellular strategies for regulating DNA supercoiling: a single-molecule perspective. *Cell.* 142:519–530.
5. Forth, S., M. Y. Sheinin, ..., M. D. Wang. 2013. Torque measurement at the single-molecule level. *Annu. Rev. Biophys.* 42:583–604.
6. Lipfert, J., M. M. van Oene, ..., N. H. Dekker. 2015. Torque spectroscopy for the study of rotary motion in biological systems. *Chem. Rev.* 115:1449–1474.
7. Kouzine, F., S. Sanford, ..., D. Levens. 2008. The functional response of upstream DNA to dynamic supercoiling in vivo. *Nat. Struct. Mol. Biol.* 15:146–154.

8. Kouzine, F., J. Liu, ..., D. Levens. 2004. The dynamic response of upstream DNA to transcription-generated torsional stress. *Nat. Struct. Mol. Biol.* 11:1092–1100.
9. Postow, L., C. D. Hardy, ..., N. R. Cozzarelli. 2004. Topological domain structure of the *Escherichia coli* chromosome. *Genes Dev.* 18:1766–1779.
10. Naumova, N., M. Imakaev, ..., J. Dekker. 2013. Organization of the mitotic chromosome. *Science.* 342:948–953.
11. Forth, S., C. Deufel, ..., M. D. Wang. 2008. Abrupt buckling transition observed during the plectoneme formation of individual DNA molecules. *Phys. Rev. Lett.* 100:148301.
12. Daniels, B. C., S. Forth, ..., J. P. Sethna. 2009. Discontinuities at the DNA supercoiling transition. *Phys. Rev. E Stat. Nonlin. Soft Matter Phys.* 80:040901.
13. Brutzer, H., N. Luzziatti, ..., R. Seidel. 2010. Energetics at the DNA supercoiling transition. *Biophys. J.* 98:1267–1276.
14. Lipfert, J., G. M. Skinner, ..., N. H. Dekker. 2014. Double-stranded RNA under force and torque: similarities to and striking differences from double-stranded DNA. *Proc. Natl. Acad. Sci. USA.* 111:15408–15413.
15. Walker, P. U., W. Vanderlinden, and J. Lipfert. 2018. Dynamics and energy landscape of DNA plectoneme nucleation. *Phys. Rev. E.* 98:042412.
16. van Loenhout, M. T., M. V. de Grunt, and C. Dekker. 2012. Dynamics of DNA supercoils. *Science.* 338:94–97.
17. Marko, J. F., and S. Neukirch. 2012. Competition between curls and plectonemes near the buckling transition of stretched supercoiled DNA. *Phys. Rev. E Stat. Nonlin. Soft Matter Phys.* 85:011908.
18. Schöpflin, R., H. Brutzer, ..., G. Wedemann. 2012. Probing the elasticity of DNA on short length scales by modeling supercoiling under tension. *Biophys. J.* 103:323–330.
19. Daniels, B. C., and J. P. Sethna. 2011. Nucleation at the DNA supercoiling transition. *Phys. Rev. E Stat. Nonlin. Soft Matter Phys.* 83:041924.
20. Cloutier, T. E., and J. Widom. 2004. Spontaneous sharp bending of double-stranded DNA. *Mol. Cell.* 14:355–362.
21. Wiggins, P. A., T. van der Heijden, ..., P. C. Nelson. 2006. High flexibility of DNA on short length scales probed by atomic force microscopy. *Nat. Nanotechnol.* 1:137–141.
22. Mathew-Fenn, R. S., R. Das, and P. A. B. Harbury. 2008. Remeasuring the double helix. *Science.* 322:446–449.
23. Vafabakhsh, R., and T. Ha. 2012. Extreme bendability of DNA less than 100 base pairs long revealed by single-molecule cyclization. *Science.* 337:1097–1101.
24. Zettl, T., R. S. Mathew, ..., J. Lipfert. 2016. Absolute intramolecular distance measurements with angstrom-resolution using anomalous small-angle X-ray scattering. *Nano Lett.* 16:5353–5357.
25. Fain, B., J. Rudnick, and S. Östlund. 1997. Conformations of linear DNA. *Phys. Rev. E.* 55:7364–7368.
26. Dittmore, A., J. Silver, and K. C. Neuman. 2018. Kinetic pathway of torsional DNA buckling. *J. Phys. Chem. B.* 122:11561–11570.
27. Allison, S. A. 1986. Brownian dynamics simulation of wormlike chains. Fluorescence depolarization and depolarized light scattering. *Macromolecules.* 19:118–124.
28. Chirico, G., and J. Langowski. 1994. Kinetics of DNA supercoiling studied by Brownian dynamics simulation. *Biopolymers.* 34:415–433.
29. Vologodskii, A., and N. Cozzarelli. 1995. Modeling of long-range electrostatic interactions in DNA. *Biopolymers.* 35:289–296.
30. Klenin, K., H. Merlitz, and J. Langowski. 1998. A Brownian dynamics program for the simulation of linear and circular DNA and other wormlike chain polyelectrolytes. *Biophys. J.* 74:780–788.
31. Ivenso, I. D., and T. D. Lillian. 2016. Simulation of DNA supercoil relaxation. *Biophys. J.* 110:2176–2184.
32. Huang, J., T. Schlick, and A. Vologodskii. 2001. Dynamics of site juxtaposition in supercoiled DNA. *Proc. Natl. Acad. Sci. USA.* 98:968–973.
33. Lipfert, J., J. W. Kerssemakers, ..., N. H. Dekker. 2010. Magnetic torque tweezers: measuring torsional stiffness in DNA and RecA-DNA filaments. *Nat. Methods.* 7:977–980.
34. Tirado, M. M., and J. G. de la Torre. 1980. Rotational dynamics of rigid, symmetric top macromolecules. Application to circular cylinders. *J. Chem. Phys.* 73:1986–1993.
35. Iniesta, A., and J. Garcia de la Torre. 1990. A second-order algorithm for the simulation of the Brownian dynamics of macromolecular models. *J. Chem. Phys.* 92:2015–2018.
36. Vologodskii, A. 2006. Brownian dynamics simulation of knot diffusion along a stretched DNA molecule. *Biophys. J.* 90:1594–1597.
37. Jian, H., A. V. Vologodskii, and T. Schlick. 1997. A combined wormlike-chain and bead model for dynamic simulations of long linear DNA. *J. Comput. Phys.* 136:168–179.
38. Lipfert, J., M. Wiggins, ..., N. H. Dekker. 2011. Freely orbiting magnetic tweezers to directly monitor changes in the twist of nucleic acids. *Nat. Commun.* 2:439.
39. Klenin, K., and J. Langowski. 2000. Computation of writhe in modeling of supercoiled DNA. *Biopolymers.* 54:307–317.
40. Britton, L. A., W. K. Olson, and I. Tobias. 2009. Two perspectives on the twist of DNA. *J. Chem. Phys.* 131:245101.
41. Lu, X.-J., and W. K. Olson. 2003. 3DNA: a software package for the analysis, rebuilding and visualization of three-dimensional nucleic acid structures. *Nucleic Acids Res.* 31:5108–5121.
42. Blanchet, C., M. Pasi, ..., R. Lavery. 2011. CURVES+ web server for analyzing and visualizing the helical, backbone and groove parameters of nucleic acid structures. *Nucleic Acids Res.* 39:W68–W73.
43. Larson, R., T. Perkins, ..., S. Chu. 1997. Hydrodynamics of a DNA molecule in a flow field. *Phys. Rev. E.* 55:1794–1797.
44. Leach, J., H. Mushfique, ..., M. J. Padgett. 2009. Comparison of Faxén’s correction for a microsphere translating or rotating near a surface. *Phys. Rev. E Stat. Nonlin. Soft Matter Phys.* 79:026301.
45. Marko, J. F. 2007. Torque and dynamics of linking number relaxation in stretched supercoiled DNA. *Phys. Rev. E Stat. Nonlin. Soft Matter Phys.* 76:021926.
46. Marko, J. F., and E. D. Siggia. 1994. Bending and twisting elasticity of DNA. *Macromolecules.* 27:981–988.
47. Nomidis, S. K., F. Kriegel, ..., E. Carlon. 2017. Twist-bend coupling and the torsional response of double-stranded DNA. *Phys. Rev. Lett.* 118:217801.
48. Wiggins, P. A., R. Phillips, and P. C. Nelson. 2005. Exact theory of kinkable elastic polymers. *Phys. Rev. E Stat. Nonlin. Soft Matter Phys.* 71:021909.
49. Jeon, J. H., J. Adamcik, ..., R. Metzler. 2010. Supercoiling induces denaturation bubbles in circular DNA. *Phys. Rev. Lett.* 105:208101.
50. Wenner, J. R., M. C. Williams, ..., V. A. Bloomfield. 2002. Salt dependence of the elasticity and overstretching transition of single DNA molecules. *Biophys. J.* 82:3160–3169.
51. Herrero-Galán, E., M. E. Fuentes-Perez, ..., J. R. Arias-Gonzalez. 2013. Mechanical identities of RNA and DNA double helices unveiled at the single-molecule level. *J. Am. Chem. Soc.* 135:122–131.

Biophysical Journal, Volume 118

Supplemental Information

Dynamics of the Buckling Transition in Double-Stranded DNA and RNA

Katharina Ott, Linda Martini, Jan Lipfert, and Ulrich Gerland

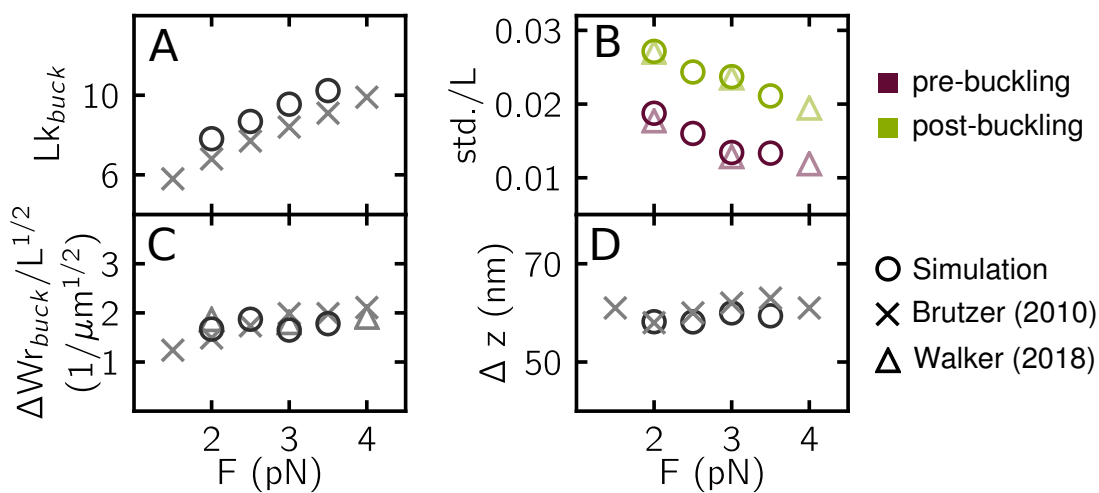


Figure S1: Equilibrium properties of the buckling transition at different forces. Simulation data is shown by grey circles. Experimental data from Ref. (1) are shown by crosses, and data taken from Ref. (2) as triangles. The experimental data from Ref. (1) are obtained using a DNA strand with the same length as the DNA in our simulation, i.e. 1.9 kbp (650 nm). For the experiments in Ref. (2) a longer DNA strand was used (7.9 kbp). In order to compare the simulation data to experiments with molecules of different contour lengths, we rescaled the parameters describing the buckling transition to length independent quantities wherever possible. (A) Position of the buckling point. (B) Width of the Gaussians describing the extension distribution, rescaled by the contour length. (C) Jump in writhe at the buckling transition, rescaled with the contour length based on the scaling behavior derived in reference (1). (D) The jump size in the extension.

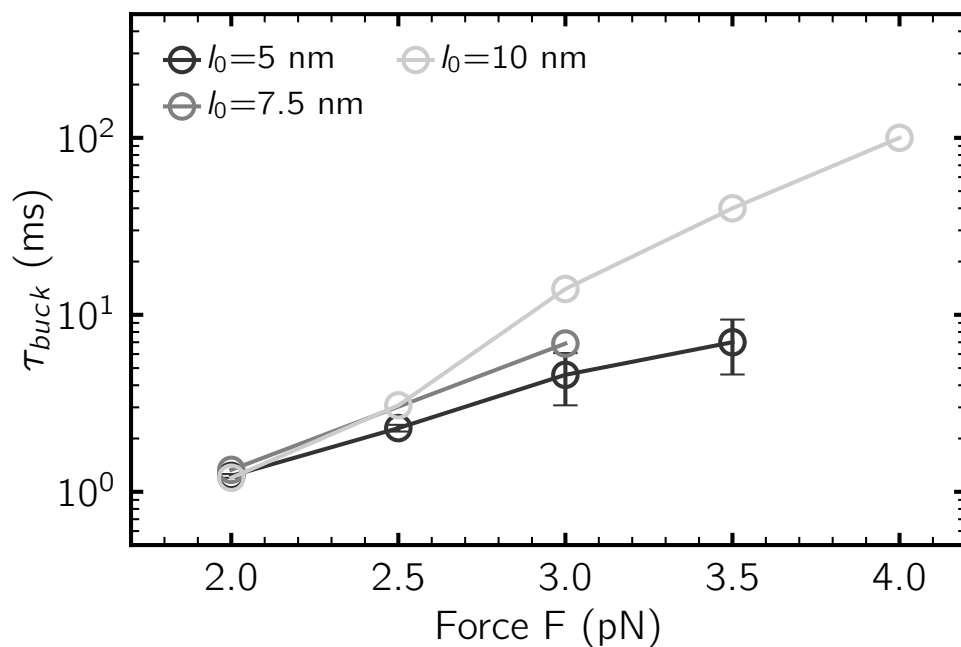


Figure S2: Comparison of buckling times calculated with different segment lengths. For low forces (~ 2 pN), the buckling times agree, whereas for higher forces significant deviations arise when the segment length is increased beyond the 5 nm segment length used in the main text. This effect is due to the fact that at higher forces, structural features of the plectoneme such as the endloop get smaller and cannot be represented with larger segments. For RNA this effect is expected to be smaller as the higher bending persistence length causes the endloop to be larger. We conclude that our simulation data for 2 and 2.5 pN is not affected by discretization effects, whereas we cannot exclude a remaining discretization effect even with our 5 nm segment length when the force is 3 pN or larger.

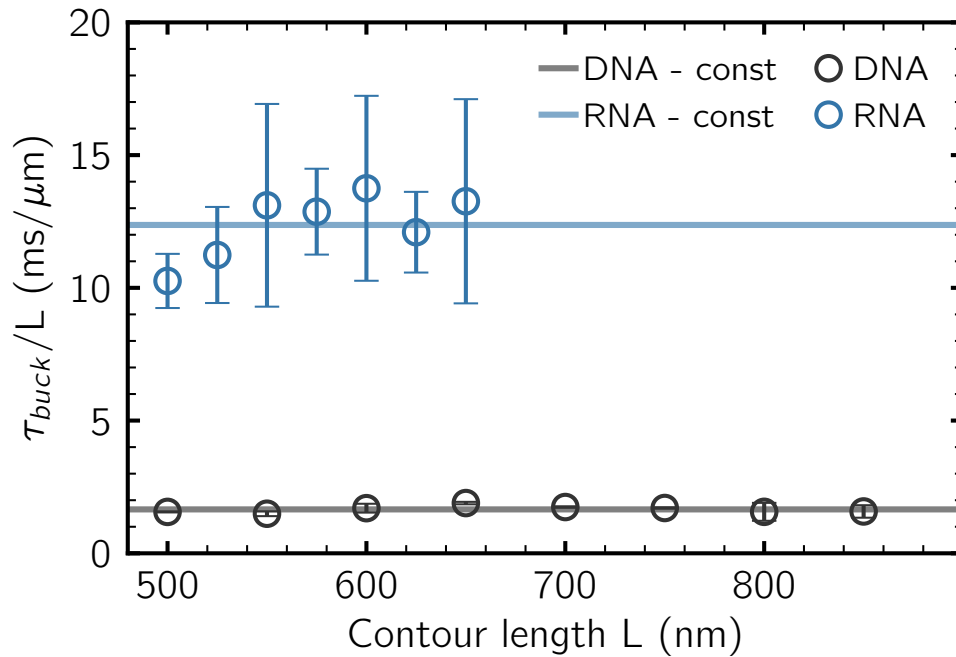


Figure S3: Dependence of the buckling time on contour length. Simulated buckling time rescaled with the contour length for DNA (grey) and RNA (blue) as a function of contour length at an external force of 2 pN. The rescaled buckling times were fit with a constant. The resulting data for DNA shows a clear linear dependence of the buckling time on the contour length. This is consistent with theoretical expectation, since since the total drag of the chain increases linearly with the contour length in the simulation, and, on average, a constant fraction of the chain has to move in order to create a plectoneme. Experiments with molecules of different contour lengths find a stronger dependence on the contour length than expected. For example, for 1.9 kbp and 7.9 kbp DNA the measured buckling times of 35 ms and 55 ms, respectively (1, 2), correspond to an increase in the buckling time by a factor of 1.57, whereas only a marginal increase by a factor 1.16 is expected after taken into account the drag coefficient of the magnetic particle (these experimental values were measured at 3 pN stretching force). However, experimental data on the dynamics of the buckling transition with different molecule lengths is still scarce (in particular for RNA), and more data will be necessary to clearly determine the experimental scaling behavior.

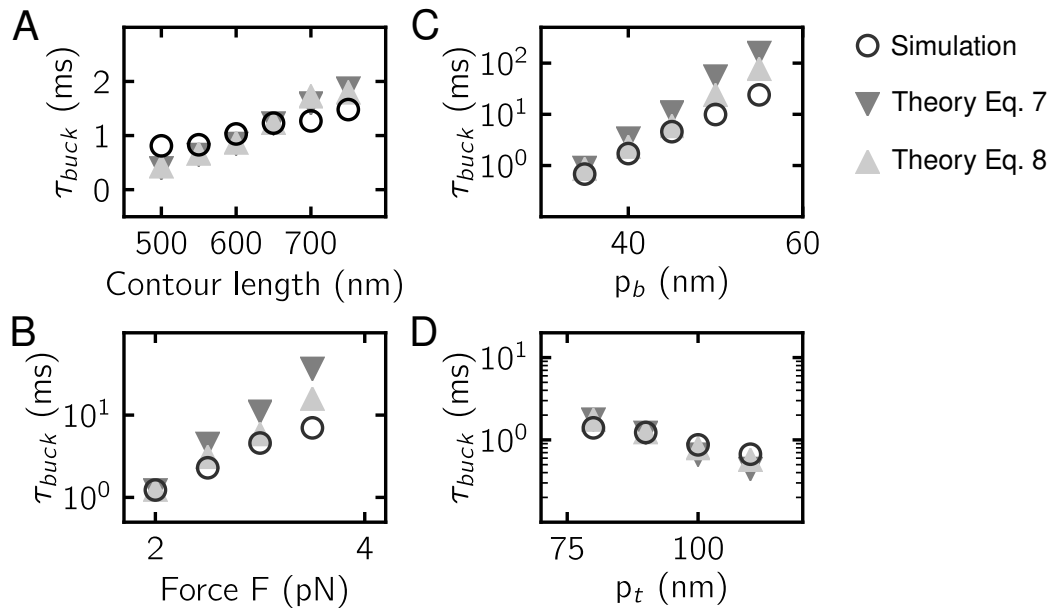


Figure S4: Comparison of analytical estimate for the buckling time with simulation. If not indicated otherwise, the following parameters are used: Contour length $L = 650$ nm, bending persistence length $p_b = 45$ nm and torsional persistence length $p_t = 90$ nm. The simulated buckling times are shown as circles. The theoretical values are calculated based on Eq. 7 (dark grey triangles) and Eq. 8 (light grey triangles). (A) Buckling time versus contour length at 2 pN external force. (B) Buckling time for different external forces. (C) Buckling time for different bending persistence lengths at 3 pN. (D) Buckling time for different torsional persistence lengths at 2 pN.

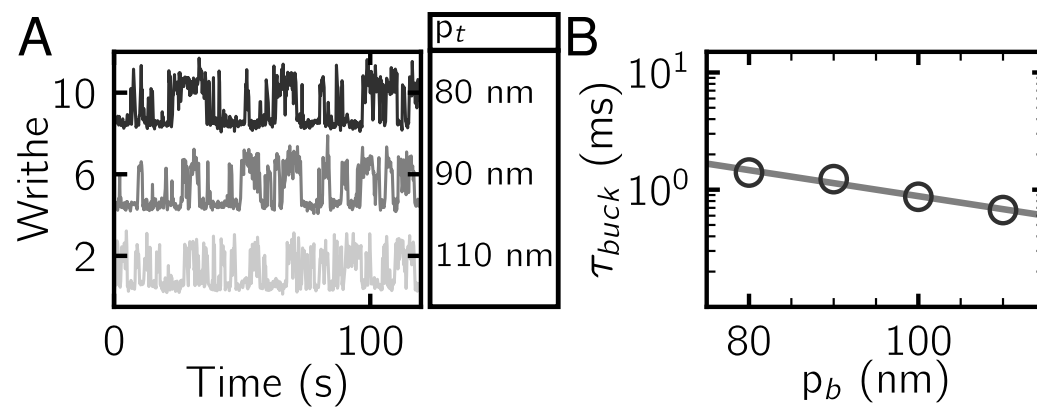


Figure S5: Dependence of buckling time on torsional persistence length. The simulation data is obtained at 2 pN external force. (A) Time traces for different torsional persistence lengths using a vertical offset of 4 for better visibility. (B) Buckling time versus torsional persistence length. The data was fit with an exponential function. The buckling time only shows a weak dependence on the torsional persistence length.

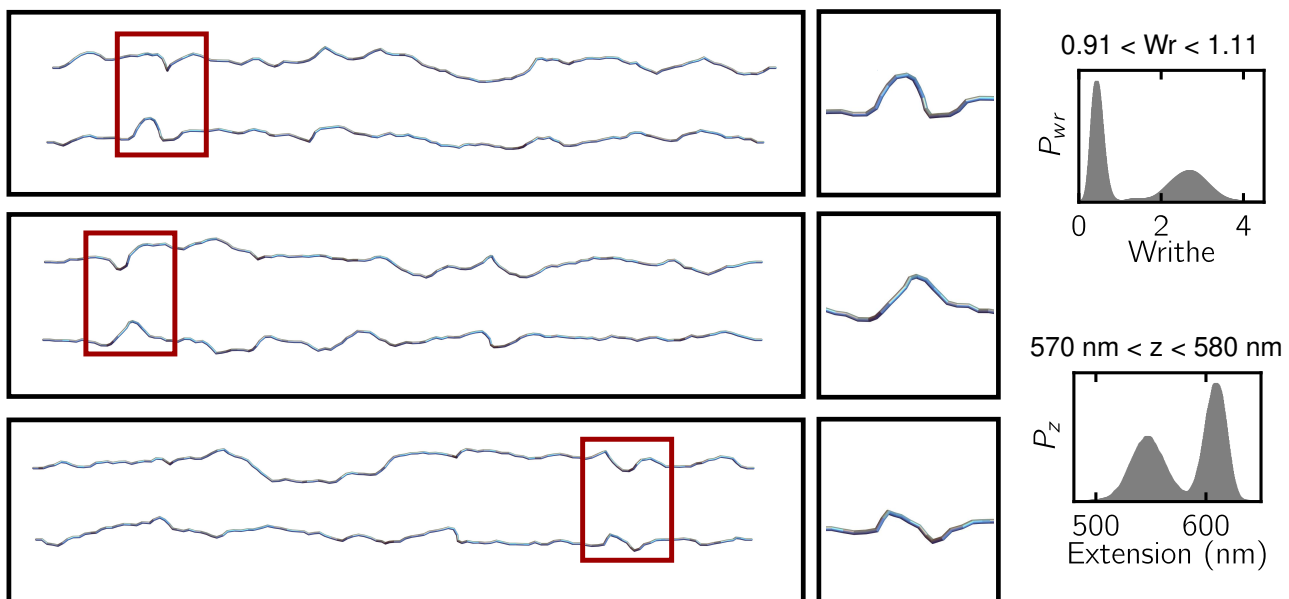


Figure S6: DNA conformations close to the transition state. Simulation data obtained at 3 pN external force. The transition state is found by searching for configurations where the linking number and the extension are within a given range and that a transition is indeed happening (which is checked by looking at the time trace of the writhe). The configurations show a solenoidal form (marked by the red rectangle), which is similar to the soliton transition state described in Refs. (3–5).

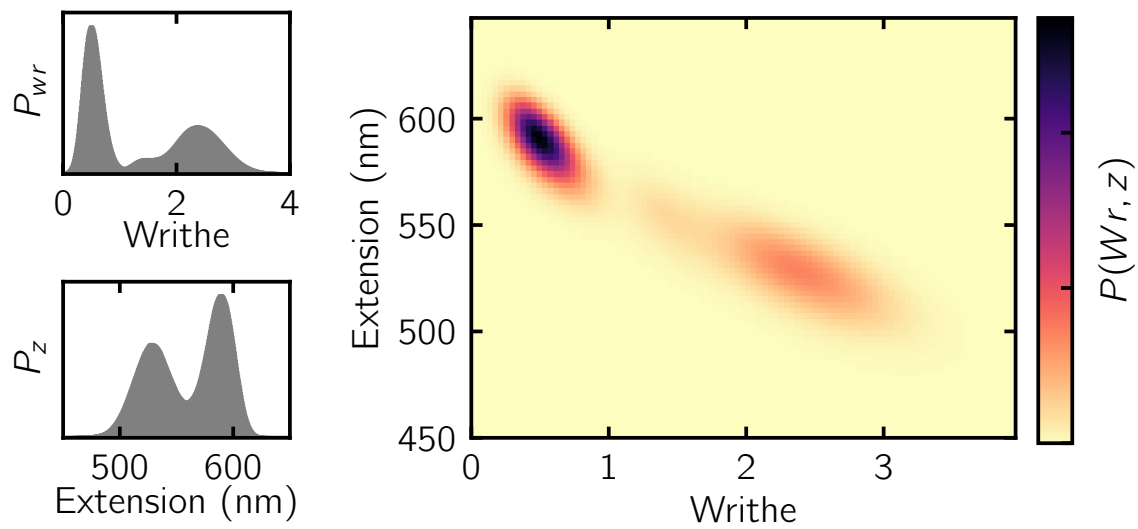


Figure S7: Extension and writhe distributions at 2 pN external force. The simulation data was obtained with DNA parameters. A small shoulder in the writhe distribution and the 2D distribution appears. This shows that the "curl" state is more populated than at 3 pN and less populated than at 1 pN.

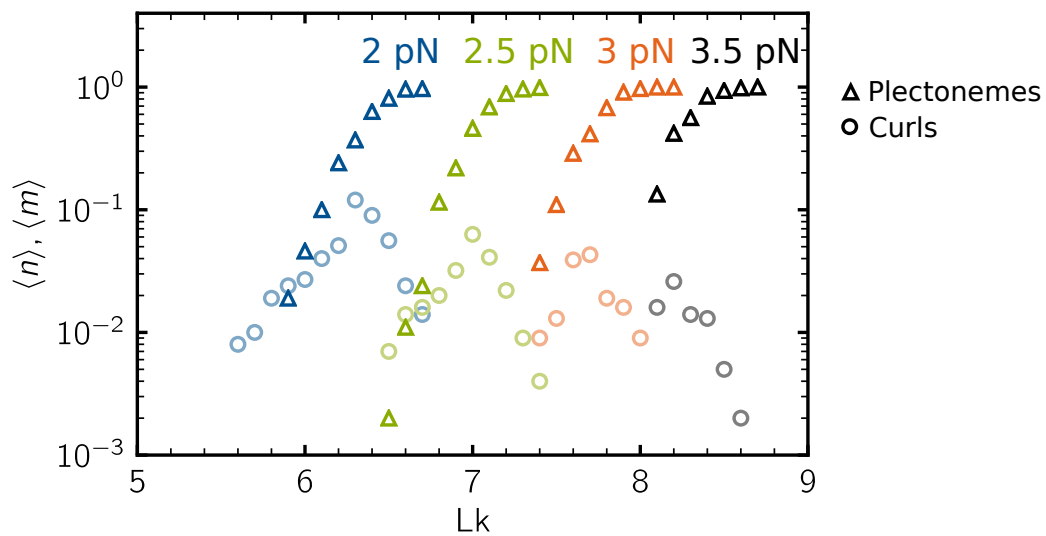


Figure S8: Occurrence of curls and plectonemes for different external forces and linking numbers. The probability to be in the curl state $\langle n \rangle$ (circles) and the probability to be in the plectoneme state $\langle m \rangle$ (triangles) were calculated for different linking numbers and forces (2 pN (blue), 2.5 pN (green), 3 pN (orange) and 3.5 pN (black)). The probabilities were obtained by fitting a Gaussian mixture model to the writhe distribution. For lower linking numbers and forces the probability of having curls increases. The resulting data are in qualitative agreement with theoretical predictions of Ref. (6).

SUPPLEMENTARY TEXT

Derivation of the twist formula

To compute the twist angle between two subsequent chain segments we define $\vec{p}_i = \vec{e}_{i-1} \times \vec{e}_i$. The twist angle is commonly defined as $\tau_i = \alpha_i + \gamma_i$, with α_i being the angle between \vec{f}_{i-1} and \vec{p}_i and γ_i being the angle between \vec{f}_i and \vec{p}_i . We define an Euler transformation to transform between the coordinate systems $\Sigma_i = (\vec{f}_i, \vec{g}_i, \vec{e}_i)$ and $\Sigma_{i-1} = (\vec{f}_{i-1}, \vec{g}_{i-1}, \vec{e}_{i-1})$ by the rotation matrix $T(\alpha_i, \beta_i, \gamma_i)$, where β_i is the angle between \vec{e}_{i-1} and \vec{e}_i . For simplicity we omit the index i in the following derivation. Using the ZYZ convention the rotation matrix is given by

$$T(\alpha, \beta, \gamma) = \begin{pmatrix} \cos \alpha \cos \beta \cos \gamma - \sin \alpha \sin \gamma & -\cos \alpha \cos \beta \sin \gamma - \cos \gamma \sin \alpha & \cos \alpha \sin \beta \\ \sin \alpha \cos \beta \cos \gamma + \cos \alpha \sin \gamma & -\sin \alpha \cos \beta \sin \gamma + \cos \alpha \cos \gamma & \sin \alpha \sin \beta \\ -\sin \beta \cos \gamma & \sin \gamma \sin \beta & \cos \beta \end{pmatrix}.$$

We transform between the coordinate systems:

$$\begin{aligned} \Sigma_i &= \Sigma_{i-1} T(\alpha, \beta, \gamma) \\ \Sigma_{i-1}^\top \Sigma_i &= \Sigma_{i-1}^\top \Sigma_{i-1} T(\alpha, \beta, \gamma) \\ \begin{pmatrix} \vec{f}_i \cdot \vec{f}_{i-1} & \vec{g}_i \cdot \vec{f}_{i-1} & \vec{e}_i \cdot \vec{f}_{i-1} \\ \vec{f}_i \cdot \vec{g}_{i-1} & \vec{g}_i \cdot \vec{g}_{i-1} & \vec{e}_i \cdot \vec{g}_{i-1} \\ \vec{f}_i \cdot \vec{e}_{i-1} & \vec{g}_i \cdot \vec{e}_{i-1} & \vec{e}_i \cdot \vec{e}_{i-1} \end{pmatrix} &= T(\alpha, \beta, \gamma) \end{aligned}$$

where we have used that Σ_{i-1} is an orthogonal matrix ($\Sigma_{i-1}^\top = \Sigma_{i-1}^{-1}$). Comparing the matrix entries we obtain

$$\begin{aligned} \vec{f}_i \cdot \vec{f}_{i-1} &= \cos \alpha \cos \beta \cos \gamma - \sin \alpha \sin \gamma \\ \vec{g}_i \cdot \vec{g}_{i-1} &= -\sin \alpha \cos \beta \sin \gamma + \cos \alpha \cos \gamma \\ \vec{f}_i \cdot \vec{g}_{i-1} &= \sin \alpha \cos \beta \cos \gamma + \cos \alpha \sin \gamma \\ \vec{g}_i \cdot \vec{f}_{i-1} &= -\cos \alpha \cos \beta \sin \gamma - \sin \alpha \cos \gamma \\ \Rightarrow \vec{f}_i \cdot \vec{f}_{i-1} + \vec{g}_i \cdot \vec{g}_{i-1} &= \cos \alpha \cos \beta \cos \gamma - \sin \alpha \sin \gamma - \sin \alpha \cos \beta \sin \gamma + \cos \alpha \cos \gamma \\ &= \cos(\alpha + \gamma)(1 + \cos \beta) \\ \vec{g}_i \cdot \vec{f}_{i-1} - \vec{f}_i \cdot \vec{g}_{i-1} &= -\cos \alpha \cos \beta \sin \gamma - \sin \alpha \cos \gamma - \sin \alpha \cos \beta \cos \gamma - \cos \alpha \sin \gamma \\ &= -\sin(\alpha + \gamma)(1 + \cos \beta) \\ \Rightarrow \frac{\vec{f}_i \cdot \vec{g}_{i-1} - \vec{g}_i \cdot \vec{f}_{i-1}}{\vec{f}_i \cdot \vec{f}_{i-1} + \vec{g}_i \cdot \vec{g}_{i-1}} &= \frac{\sin(\alpha + \gamma)}{\cos(\alpha + \gamma)} \\ &= \tan(\alpha + \gamma) \end{aligned}$$

Model for the buckling time

To interpret the simulated buckling times, we need an expression for the energy barrier of the buckling transition. In our simulation we observed that the transition state has a 'soliton like' form (see Figure S6), similar to analytical predictions by (3, 4). Therefore we base our analysis on the expression for the energy barrier given by (3), which was found using an inextensible wormlike chain model. The energy barrier is defined by the local energy minimum corresponding to a straight chain with the twist given by the linking number and a 'soliton-like' transition state. Ref. (3) defines the following length scales,

$$a = \sqrt{p_b k_B T / F} \quad (1)$$

$$b = 2p_b k_B T / \Gamma \quad (2)$$

$$l = (a^{-2} - b^{-2})^{-1/2} \quad (3)$$

where Γ is the torque. The linking number at the buckling transition is given by

$$Lk_{\text{buck}} = \frac{\Gamma L}{2\pi p_t k_B T} + Wr_{\text{buck}} \quad (4)$$

where the writhe at the buckling transition is given by

$$Wr_{\text{buck}} = \frac{2}{\pi} \arctan \left(\frac{b}{l} \tanh \left(\frac{L}{2l} \right) \right). \quad (5)$$

The linking number Lk_{buck} cannot be calculated directly from this theory and therefore we use the observed linking number in the simulation to calculate the torque Γ . The energy barrier is then given by

$$\Delta E_b = \frac{8p_b k_B T}{l} \tanh \left(\frac{L}{2l} \right) - 2\pi W r_{\text{buck}} \left(\Gamma + \frac{\pi p_t k_B T}{L} W r_{\text{buck}} \right). \quad (6)$$

To get from the energy barrier to the buckling time, we use Kramer's transition state theory in one dimension, which leads to a buckling time of the form

$$\tau_{\text{buck}} = C \gamma \exp \left(\frac{\Delta E_b}{k_B T} \right). \quad (7)$$

For the drag coefficient γ we use the expression given in the main text. C is the curvature parameter in Kramer's theory defined via the curvature at the energy minimum and the curvature at the transition state, but the value cannot be directly and simply extracted from the theory. In practice C is dependent on the different parameters (like external force, bending persistence length and others) but as a simple approximation we first leave it as a constant fit parameter (Figure S4 dark grey triangles). To additionally account for the change in C we reconstruct the energy landscape from the extension histogram via $\Delta G(z) = -k_B T \ln P(z)$. Using this energy landscape we can approximate the curvature C_z . This curvature does not correspond directly to the curvature in Eq. 7 and therefore we introduce it as a factor C_z/C_{DNA} where C_{DNA} is the curvature parameter of the DNA energy landscape at 2 pN external force. This allows us to use the same parameter C with and without correction factor. The buckling time is then calculated including this factor:

$$\tau_{\text{buck}} = C \frac{C_z}{C_{\text{DNA}}} \gamma \exp \left(\frac{\Delta E_b}{k_B T} \right) \quad (8)$$

It is important to note that any entropic contributions were neglected in this calculation.

The calculated buckling times agree well with our simulated buckling times (Figure S4) and reproduce all the trends observed in the simulation. That is an increase in the buckling time with the force (Fig. S4 B), an increase of the buckling time with the bending persistence length (Fig. S4 C) and a decrease in the buckling time with increasing torsional persistence length (Fig. S4 D). Including the correction due to the change in curvature for these parameters improves the agreement.

SUPPORTING REFERENCES

1. Brutzer, H., N. Luzzietti, D. Klaue, and R. Seidel, 2010. Energetics at the DNA supercoiling transition. *Biophys J* 98:1267–1276.
2. Walker, P. U., W. Vanderlinden, and J. Lipfert, 2018. Dynamics and energy landscape of DNA plectoneme nucleation. *Physical Review E* 98:042412.
3. Daniels, B. C., and J. P. Sethna, 2011. Nucleation at the DNA supercoiling transition. *Physical Review E* 83:041924.
4. Fain, B., J. Rudnick, and S. Östlund, 1997. Conformations of linear DNA. *Physical Review E* 55:7364.
5. Dittmore, A., J. Silver, and K. C. Neuman, 2018. Kinetic Pathway of Torsional DNA Buckling. *J Phys Chem B* 122:11561–11570.
6. Marko, J. F., and S. Neukirch, 2012. Competition between curls and plectonemes near the buckling transition of stretched supercoiled DNA. *Physical Review E* 85:011908.